ADVANCED MATERIALS
www.advmat.de

Colloidal Ink Engineering for Slot-Die Processes to Realize Highly Efficient and Robust Perovskite Solar Modules

Sushil Shivaji Sangale, Hyeonsu Son, Sang Wook Park, Pramila Patil, Tae Kyung Lee, Sung-Nam Kwon,* and Seok-In Na**

Perovskite solar cells (PSCs) have emerged as a promising alternative to silicon solar cells, but challenges remain in developing perovskite inks and processes suitable for large-scale production. This study introduces a novel approach using colloidal inks incorporating toluene and chlorobenzene as co-antisolvents for PSC fabrication via slot-die process. It is found that colloidal inks that are strategically engineered can significantly improve the rheological properties of perovskite inks, leading to enhanced wettability and high-quality film formation. The formation of large colloids such as α cubic perovskite, δ hexagonal perovskite and transition intermediate phases promotes heterogeneous nucleation and lowers activation energy for crystallization, resulting in superior crystal growth and improved film morphology. Notably, the co-solvent enhances the FA-PbI_3 binding energy and weakens the dimethyl sulfoxide coordination, which is more thermodynamically favorable for perovskite crystallization. This colloidal strategy yields devices with a maximum efficiency of 21.32% and remarkable long-term stability, retaining 77% of initial efficiency over 10115 h. The study demonstrates the scalability of this approach, achieving 20.26% efficiency in lab-scale minimodules and 19.15% in larger convergence minimodules. These findings provide an understanding of the complex relationship between ink composition, rheological properties, film quality, crystallization kinetics, and device performance.

1. Introduction

During the past decade, remarkable progress has been achieved in perovskite solar cells (PSCs) technology, driven by continuous efforts to enhance its efficiency and stability. Today, PSCs are considered a promising alternative to traditional silicon solar cells due to their high power conversion efficiency (PCE) of over 26% and cost-effective manufacturing processes.[1] However, such high efficiencies have primarily been achieved in small-area devices with active areas typically <0.1 cm^2. Extending these efficiencies to larger module levels remains a key challenge. Various strategies have been employed to address this issue, including improving perovskite phase stability,[2] employing mixed perovskite compositions,[3] additive engineering,[4] and interfacial modifications to minimize defects and enhance stability,[5] and improve scalability and efficiency. For example, Yang et al. employed diphenyl sulfoxide (DPSO) to stabilize wet precursor films, achieving a PCE of 16.63% on a 20.77 cm^2 active area.[6] Similarly, Bu et al. utilized N-methylpyrrolidone (NMP) to coordinate with lead iodide and incorporated methylammonium chloride additives, achieving a PCE of 20.42% (17.1 cm^2 aperture area).[2] Yue et al. introduced the green additive N-methyl-2-piperidone to modify the perovskite precursor, attaining a PCE of 21% (10 cm^2 aperture area).[7] Despite these advancements, module-level efficiencies still suffer from 15–20% losses for aperture areas of 10–30 cm^2. Additionally, the development of affordable perovskite materials and precursor inks suitable for large-scale production and the implementation of environmentally friendly manufacturing processes remain hurdles on the path to commercialization.

A comprehensive understanding of perovskite ink chemistry is an essential prerequisite to overcoming these challenges. In line with this, interest in the colloidal chemistry of perovskite inks has recently increased, and studies have been conducted in widely used highly polar solvent systems such as N,N-dimethylformamide (DMF), and dimethyl sulfoxide (DMSO).[8] As a result, recent research has shown that perovskite inks are not an ideal solution in which the perovskite precursor is completely dissolved, but rather an imperfect solution containing

S. S. Sangale, S.-N. Kwon, S.-I. Na
Department of Flexible and Printable Electronics
LANL-JBNU Engineering Institute-Korea
Jeonbuk National University
Jeonju 54896, Republic of Korea
E-mail: dasom2u@jbnu.ac.kr; nsi@jbnu.ac.kr
H. Son, T. K. Lee
Department of Materials Engineering and Convergence Technology
Gyeongsang National University (GNU)
501 Jinju-daero, Jinju 52828, Republic of Korea
E-mail: tklee8865@gnu.ac.kr
S. W. Park, T. K. Lee
School of Materials Science and Engineering
Gyeongsang National University (GNU)
501 Jinju-daero, Jinju 52828, Republic of Korea
P. Patil
Helmholtz-Zentrum Berlin für Materialien und Energie GmbH Hahn-Meitner-Platz 1
D-14109 Berlin, Germany

The ORCID identification number(s) for the author(s) of this article can be found under https://doi.org/10.1002/adma.202420093

DOI: 10.1002/adma.202420093

various forms of incompletely dissolved phases, e.g. colloids.[8c,9] It has also been reported that the thermodynamic driving force for crystallization can be finely controlled by tuning the interactions between colloidal particles through changes in additive content, pH of solution, and supersaturation conditions.[8a,b] In particular, colloidal properties, including colloidal size distribution and colloidal concentration, have been reported to significantly influence the defect concentration, growth direction, crystallinity, morphology of perovskite films, as well as the final device performance.[10] For example, to deposit defect-low perovskite films, stoichiometric δ-phase lead formamidinium iodide (δ-$FAPbI_3$) powders were synthesized by mechanochemical methods to be used as high-purity precursors, and it was demonstrated that upon redissolution, the pre-synthesized δ-$FAPbI_3$ precursors formed micrometer-sized colloids, favoring crystallization by spontaneous heterogeneous nucleation.[11] Further, it was reported that substitution of lead iodide (PbI_2) with lead acetate ($PbAc_2$) in perovskite precursor inks increased the size of $CsPbI_3$ colloids in the precursor and reduced the nucleation energy barrier, resulting in the formation of dense, uniform, and pinhole-free $CsPbI_3$ perovskite films.[12] On the other hand, Grätzel et al. introduced a co-solvent dilution strategy by adding tetrahydrofuran (THF) to a mixed solvent of DMF and DMSO. This approach turned the interaction between Pb^{2+} and the solvents and led to the stabilization of lead polyhalide colloids in perovskite precursor inks, resulting in the production of high-quality perovskite films and extended processing for large-scale modules.[13] Therefore, the colloidal strategy can be one choice for scale-up and commercialization.

Unlike small devices, in actual scale-up processes, the surface tension, viscosity, boiling point, vapor pressure, etc. of the solvent have a significant impact on the surface uniformity and PCE of large-area perovskite devices, so it is important to consider the rheological properties of colloidal inks. In this regard, the microfluidics of perovskite inks are having a profound impact on the large-scale manufacturing of solar cells across a variety of technologies, including blade coating,[14] screen printing,[15] roll-to-roll printing,[16] and slot-die coating (SD).[17] Among these coating techniques, SD emerges as a highly promising technology for manufacturing PSCs, Burkitt et al. have defined a comprehensive processing framework that includes various factors such as coating speed, coating interval, flow rate, surface tension, and ink viscosity.[18] Nevertheless, an approach that addresses specific process parameters is still needed to achieve stable and consistent perovskite film deposition. In particular, the rheological properties of the ink, including surface tension and viscosity, play a key role in ensuring the initial formation of a uniform perovskite wet film in the SD process. For instance, the viscosity of the perovskite ink was controlled by incorporating acetonitrile (ACN) into a 2-methoxyethanol-based formamidinium lead triiodide ($FAPbI_3$) precursor ink, resulting in the formation of a smooth perovskite film with no ribbing effect and minimodules with a PCE of 17.1%.[19] In addition, in our previous work, we applied the strategy of using 1,2-dichlorobenzene (DCB) as a modifier to control the rheological properties while producing locally supersaturated colloids. The resulting wettability enhancement and colloid formation allowed the formation of dense, large-grained perovskite films, ultimately leading to the fabrication of minimodules with 17.66% PCE.[20] In short, the rheological properties of perovskite precursor inks play an important role in the formation of perovskite films that crystallize from wet films. However, ink rheology and the utilization of colloidal perovskite ink strategies have not been studied in depth. Therefore, to achieve scale-up for commercialization, including large-area SD, significant effort is required to optimize perovskite inks suitable for efficient and reliable PSC manufacturing, including rheological properties such as surface tension, viscosity, and colloids.

In this study, we demonstrate a novel approach to fabricating high-efficiency, highly stable PSCs and minimodules using an SD process based on colloidal inks. By incorporating the antisolvents toluene (TL) and chlorobenzene (CB) as modulator solvents, a colloidal ink system was formulated that exhibits superior rheological properties compared to conventional precursor inks (CPI). This colloidal ink improves wettability, while the transition intermediate phases promote heterogeneous nucleation and lower the activation energy for crystallization, resulting in the formation of high-quality perovskite films. Additionally, density functional theory (DFT) calculations revealed that the inclusion of TL+CB co-antisolvents increased the binding energy between the FA cation and PbI_3 anion, making the crystallization process more thermodynamically favorable. Through a comprehensive analysis of ink composition, rheological properties, film quality, crystallization kinetics, and computational modeling and analysis, the intricate relationship between these factors and device performance was elucidated. Our optimized colloidal ink yields devices with a maximum efficiency of 21.32% and remarkable long-term stability. Furthermore, it has proven to be highly scalable, achieving efficiencies of 20.26% in a 2.7 cm^2 lab-scale minimodule and 19.15% in an 8.64 cm^2 converged minimodule. These results not only provide valuable insights into fundamental aspects of colloidal ink-based perovskite film formation but also suggest a promising approach for the commercialization of high-efficiency, highly stable perovskite solar cells and modules.

2. Results and Discussion

2.1. Performance of Colloidal Ink-Based Devices

Figure 1a illustrates the preparation process of the colloidal ink and the subsequent formation of a perovskite film using the SD coating method. To prepare the CPI, a precursor with the composition of $Cs_{0.175}FA_{0.750}MA_{0.075}Pb(I_{0.880}Br_{0.120})_3$ was first mixed in DMSO to 1.45 M. Following this, for the preparation of colloidal inks, TL and CB, one of the antisolvents, were added to DMSO-based perovskite precursor inks in appropriate amounts as additives, thereby inducing supersaturation of the precursor solution and formation of nanocrystals, i.e., colloids. The following criteria were employed in the selection of these antisolvents: a) the antisolvent must be highly miscible with the host solvent (DMSO) to prevent phase separation, b) to improve the wettability of DMSO-based precursor inks with high surface tension and viscosity, the antisolvent should have low surface tension and viscosity, c) it should have a low boiling point (BP) and high vapor pressure (VP) to facilitate solvent extraction and removal, d) it should have a low dielectric constant and dipole moment to induce supersaturation and nanocrystal formation by properly breaking the perovskite-DMSO intermediate phase.

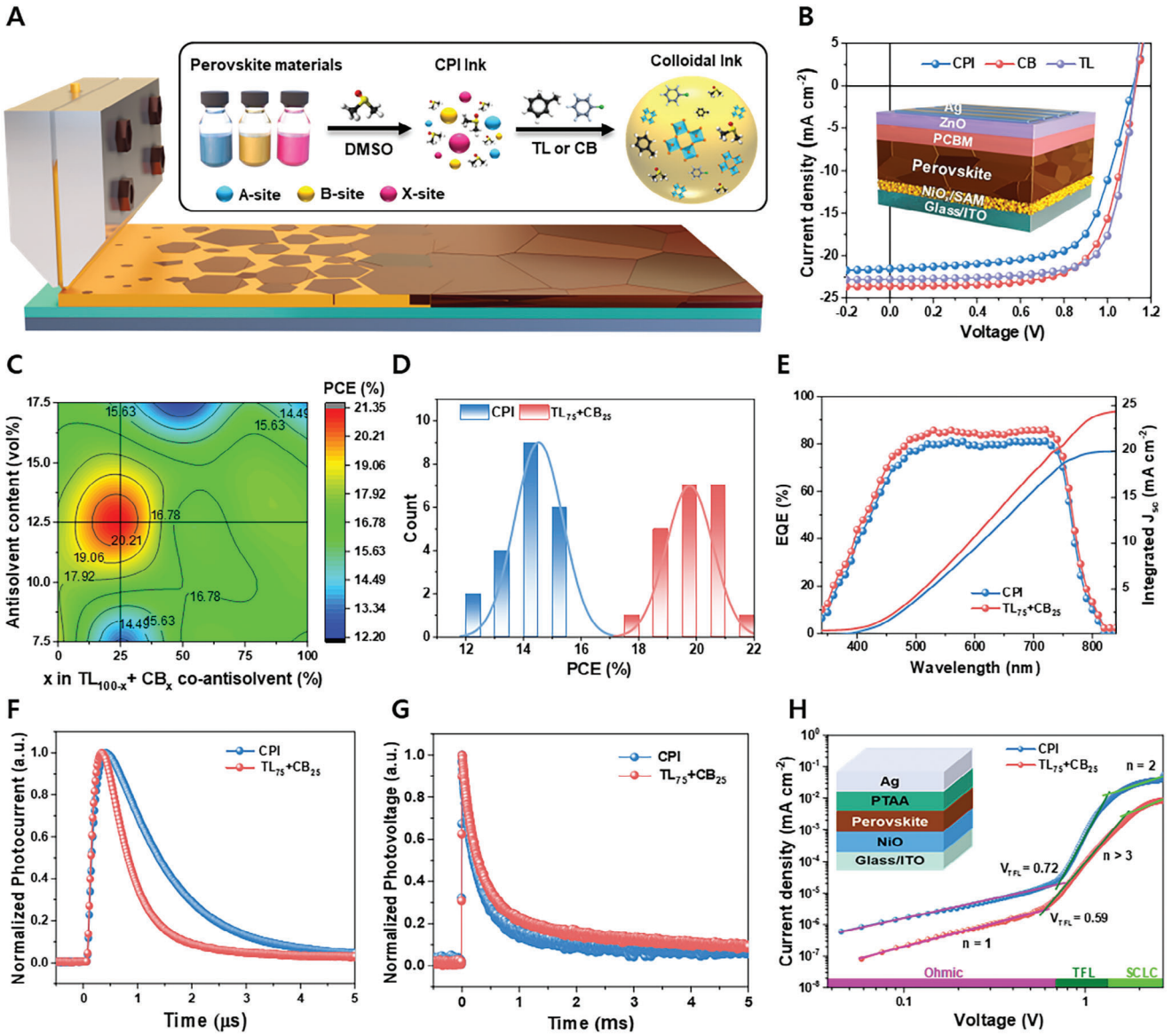

Figure 1. a) Schematic illustration of the perovskite film coating process using colloidal ink formulation and slot-die technique. b) Current–voltage (*J*–*V*) curves of PSCs with CPI and colloidal inks containing TL or CB (Inserted figure exhibits the device architecture based on the p-i-n structure). c) PCE contour plot of PSCs as a function of the content and ratio of CB and TL. d) PCE histogram of the PSCs with CPI and colloidal inks containing TL_{75}+CB_{25}. e) External quantum efficiency (EQE) of the PSCs with CPI and colloidal inks containing TL_{75}+CB_{25}. f, g) Transient photocurrent (TPC) and transient photovoltage (TPV) curves of the CPI and colloidal inks containing TL_{75}+CB_{25}. h) Space charge-limited current (SCLC) measurement of the CPI and colloidal inks containing TL_{75}+CB_{25}.

Detailed physicochemical properties of TL and CB, including surface tension, viscosity, boiling point, vapor pressure, etc. are given in Table S1 (Supporting Information). In such an ink system, DMSO forms an intermediate phase through strong coordination bonds with Pb^{2+} in perovskite, and as is well known, the added antisolvent is expected to induce nanocrystal formation by breaking these coordination bonds.[21] Thus, the colloidal ink ultimately consists of perovskite intermediate phases, perovskite nanocrystals, DMSO, TL, and CB. As shown in Figure S1 (Supporting Information), a colloidal ink formulated with the appropriate amounts of TL and CB produces a clear yellow solution that is identical to CPI. When the size distribution of colloids in colloidal inks was determined by dynamic light scattering (DLS) measurements, it was found that colloidal inks contain more colloids in the size range of 1000 nm and above compared to the CPI. This is mainly due to the nanocrystallization of the precursor solution, and the generation of large colloids gradually increases with higher antisolvent content. The formation of colloids depending on the content of antisolvents, and their respective ratios will be discussed in more detail in Section 2.3. In addition, detailed information on the experimental procedures related to the formulation of perovskite precursor inks and the SD-based device fabrication process can be found in the Supporting Information.

First, in order to investigate the correlation between colloidal inks containing 7.5 to 17.5 vol% antisolvent and device performance, SD-based inverted structure (p-i-n) PSCs were fabricated, and photoelectrical analysis was undertaken. Figure 1b shows the corresponding representative current–voltage (*J*–*V*) curves of PSCs with CPI and colloidal inks containing TL or CB. Detailed *J*–*V* curves for different TL or CB contents are plotted in Figure S2 (Supporting Information), and the associated photovoltaic parameters are listed in Table S2 (Supporting Information). The CPI-based PSC exhibited a low PCE of 15.66%, while the colloidal ink-based PSC containing CB and TL exhibited improved PCE of 18.34% and 18.90%, respectively, where the content of CB and TL was equalized to 12.5 vol%. This result means that the optimal content for both CB and TL is 12.5 vol%. Further, the device performance was evaluated as a function of the mixing ratio of CB and TL to identify the synergistic effect of adding a mixture of two antisolvents (TL+CB) with different physicochemical properties. As shown in Figure 1c and Figure S3 (Supporting Information), which show contour plots and corresponding *J*–*V* as a function of the content and ratio of CB and TL, PSCs based on colloidal inks containing optimized amounts of co-antisolvent (TL+CB) showed superior efficiency compared to CPI as well as single TL and CB-based colloidal inks. In particular, the highest efficiency of 21.32% in combination with a high short-circuit current density (J_{SC}) of 25.38 mA cm^{-2}, open-circuit voltage (V_{OC}) of 1.15 V, and fill factor (FF) of 72.56% was achieved with the addition of 12.5 vol% of a co-antisolvent containing a 75:25 ratio of TL and CB (TL_{75}+CB_{25}) (Figure S4 and Table S3, Supporting Information). The PCE histogram of the 20 devices shows that the colloidal ink-based devices with TL_{75}+CB_{25} (average PCE 20.20%) have reproducibility in the higher efficiency distribution compared to the CPI-based devices (average PCE 14.52%) (Figure 1d). Furthermore, we analyzed the impact of humidity on device performance. The results indicate that there was no significant impact on film quality or efficiency, even though fluctuations in humidity (Figure S5, Supporting Information). The external quantum efficiency (EQE) spectra showed that the efficiency improvement of the colloidal ink-based devices containing TL_{75}+CB_{25} as compared to the CPI-based device was attributed to the superior photon-to-current conversion efficiency across the entire wavelength range (Figure 1e).

Transient photocurrent (TPC) and transient photovoltage (TPV) analyses, which can provide insightful understanding of photoinduced charge carrier dynamics, including charge carrier lifetime characteristics and time-dependent charge extraction under operating conditions, have provided evidence for the factors responsible for this efficiency improvement. As shown in Figure 1f,g, the TPC and TPV decay times of colloidal ink-based PSCs with TL_{75}+CB_{25} were 2.08 µs and 2.79 ms, respectively, which are shorter and longer than those of CPI-based PSCs, indicating that charge extraction-transport and charge lifetime are enhanced and non-radiative recombination is reduced in colloidal-based devices.[20,22] Further, space charge-limited current (SCLC) measurements showed that the enhancement of charge carrier dynamics in colloidal ink-based PSCs with TL_{75}+CB_{25} can be attributed to the lower trap density. When SCLC analysis was performed using hole-only devices (ITO/NiO_x/perovskite/PTAA/Ag), the CPI- and colloidal ink (TL_{75}+CB_{25})-based devices exhibited V_{TFL} values at 0.72 and 0.59 V, respectively, and the trap densities of 5.58×10^{15} and 4.58×10^{15} cm^{-3} were calculated correspondingly (Figure 1h). This indicates that colloidal ink-based perovskite films with TL and CB have lower trap densities compared to CPI-based perovskite films, resulting in reduced trap-assisted charge carrier recombination and improved PSC performance.[23] From this, it can be inferred that co-antisolvent-based colloidal inks containing TL and CB improve the quality of SD-based perovskite films, leading to improved device efficiency.

2.2. Perovskite Films and Rheological Properties of Colloidal Inks

Figure S6 (Supporting Information) shows low-magnification optical microscopy images depending on the colloidal ink composition, demonstrating the overall coating quality of the perovskite film. For both colloidal inks containing CB (represents TL_0+CB_{100}) or TL (represents TL_{100}+CB_0), it can be clearly seen that the size of the grains has increased compared to the CPI-based perovskite film, with the grain size increasing from 20–50 µm for CPI to 50–90 µm for CB, 50–120 µm for TL, and 80–150 µm for TL_{75}+CB_{25}. The general trend with colloidal inks is to increase grain size, but it has been found that film quality varies significantly depending on the content and composition of CB or TL. As shown in the high-magnification field emission scanning electron microscopy (FE-SEM) images of Figure S7 (Supporting Information), for the colloidal ink containing 12.5 vol% antisolvent, dense film morphology and no pinholes can be observed, whereas for colloidal inks containing less or more antisolvent, including CPI, pinholes, cavities, and cracks (highlighted by an orange circle) appear at the grain boundaries and grain bodies. Furthermore, as shown in **Figure 2**a, the colloidal ink containing 12.5 vol% co-antisolvent in the TL_{75}+CB_{25} composition formed a dense film with no pinholes, whereas the colloidal inks containing single antisolvent or more than 25% CB produced pinholes, cavities, and cracks at the grain boundaries and grain bodies. As a result, it can be concluded that the colloidal ink containing 12.5 vol% of antisolvent in the TL_{75}+CB_{25} composition is the optimal condition for the formation of a high-quality perovskite film, which is consistent with the change in device performance.

X-ray diffraction (XRD) analysis was used to qualify the crystallographic differences in colloidal ink-based perovskite films for different co-antisolvent contents and ratios. As shown in Figure S8 (Supporting Information), all perovskite films using colloidal inks showed a diffraction pattern typical of cubic perovskite crystals, with an additional unreacted PbI_2 peak at 12.7° in the case of CPI.[24] Importantly, as shown in Table S4 (Supporting Information), the trend of the full width at half maximum (FWHM) was similar to the surface morphology of the perovskite films, indicating that the colloidal ink containing 12.5 vol% antisolvent with TL_{75}+CB_{25} composition resulted in the formation of high-quality perovskite films with the best crystallinity. In steady-state photoluminescence (PL) analysis (Figure S9, Supporting Information), which indirectly shows the defect density and charge recombination characteristics within the perovskite film, the perovskite film with TL_{75}+CB_{25} had the highest spectral intensity with a slight blue shift, which suggests that non-radiative charge recombination was more suppressed as the defect density decreased.[25] This finding is further supported by time-resolved photoluminescence spectra (TRPL) (Figure S10, Supporting Information). When the

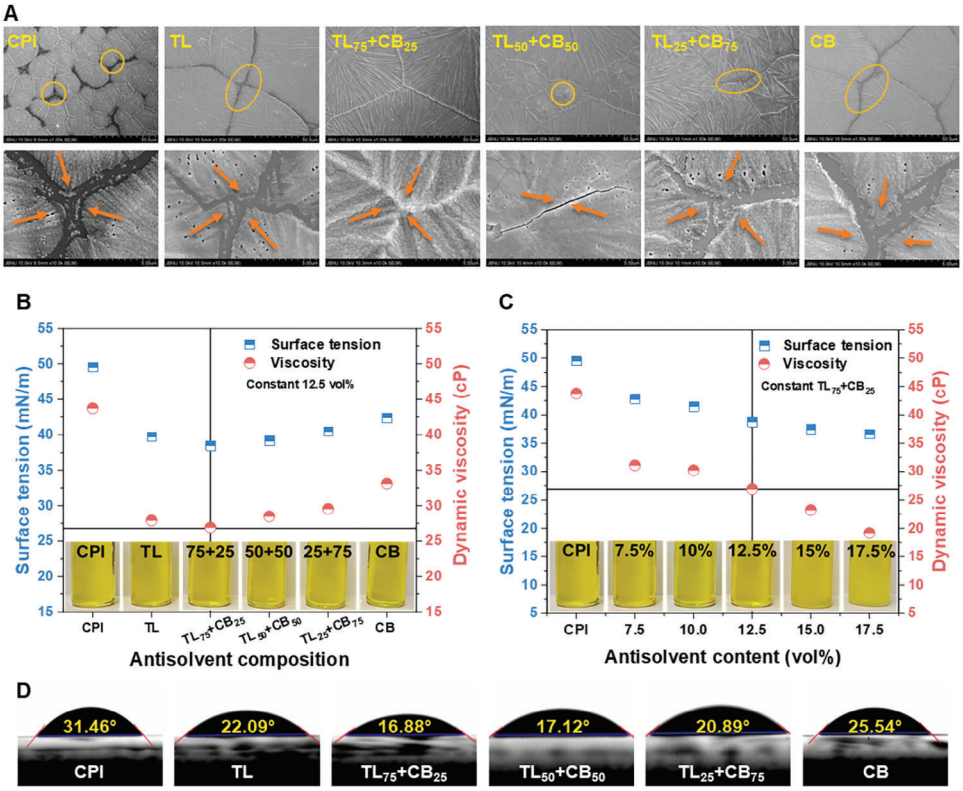

Figure 2. a) Field emission scanning electron microscopy (FE-SEM) images of perovskite films prepared with CPI and different TL+CB ratios. b) Variations in surface tension and dynamic viscosity of perovskite colloidal inks with different TL and CB ratios. c) Variations in surface tension and dynamic viscosity of perovskite colloidal inks with various TL_{75}+CB_{25} contents. d) Contact angles of perovskite colloidal inks with different TL and CB ratios.

average fluorescence lifetime (τ_w) was measured from the TRPL spectra using a bi-exponential decay function (Table S5, Supporting Information), the perovskite film with TL_{75}+CB_{25} exhibited a slower τ_w (≈63 ns) compared to the CPI-based perovskite film (τ_w ≈ 40 ns). This shows a reduction in non-radiative recombination of colloidal ink-based perovskite films containing co-antisolvent (TL_{75}+CB_{25}), which can be inferred to be due to the suppression of defects in the film by the formation of dense, large grains with no pinholes and good crystallinity.

To understand the correlation between the physicochemical properties of colloidal inks and the formation kinetics of SD-based perovskite films, the rheological properties of the inks, such as surface tension (σ) and dynamic viscosity (η), were analyzed as a function of the content and composition of the antisolvent in the colloidal ink formulations exhibiting optimal perovskite film and efficiency properties. As shown in Figure 2b,c, the σ and η of colloidal inks decreased with the addition of CB or TL, especially TL_{75}+CB_{25} showed the lowest σ (38.52 mN m^{-1}) and η (26.93 cP) values, and the σ and η decreased further with the increase of TL_{75}+CB_{25} co-antisolvent content. This change in σ and η was more evident in the change in contact angle (θ). As shown in Figure 2d and Figure S11 (Supporting Information), the θ measured for the NiO/MeO-2PACz hole transport layer was the lowest at 16.88° for the colloidal ink with TL_{75}+CB_{25} co-antisolvent, and further θ showed a decreasing trend with increasing TL_{75}+CB_{25} co-antisolvent content. From this, the free energy of adhesion, i.e., the work required to separate the liquid from the solid surface, was calculated by the Young-Dupre equation, $W = \gamma_L(1 + \cos\theta)$,[26] where CPI and TL_{75}+CB_{25} denoted approximately 91.83 and 75.38 mN m^{-1}, respectively. The results allow us to predict the degree of wettability and the resulting change in Gibbs free energy, indicating that TL_{75}+CB_{25} with lower values has better wettability and can promote crystallization than CPI.[27] Based on the previous perovskite film and device performance characteristics, these results suggest that a colloidal ink containing 12.5 vol% of TL_{75}+CB_{25} co-antisolvent with a σ of 38.52 mN m^{-1} and a η of 26.93 cP is optimal for the formation of SD-based perovskite films and that in other cases, the surface tension and viscosity of the colloidal ink are too high or too low to form good perovskite thin films. This is because when the perovskite ink has the appropriate surface tension and viscosity, the perovskite precursor dispensed through the SD process can form a uniform wet film of ideal thickness without pinholes that dominate the quality of the perovskite film. These results also were consistent with UV analysis of wet films showing high absorbance in thick and dense films (Figure S12, Supporting Information). Further, UV-vis light absorption spectra for fully annealed perovskite films show a slight red shift,[28] indirectly showed that the thickness of perovskite films increases in colloidal inks containing antisolvents (Figure S13, Supporting Information),[28b] which was consistent with the film thickness trends measured with a contact surface profiler (alpha-step) (Tables S6 and S7, Supporting Information). The CPI-based perovskite film was thin with an average thickness of 314 nm and

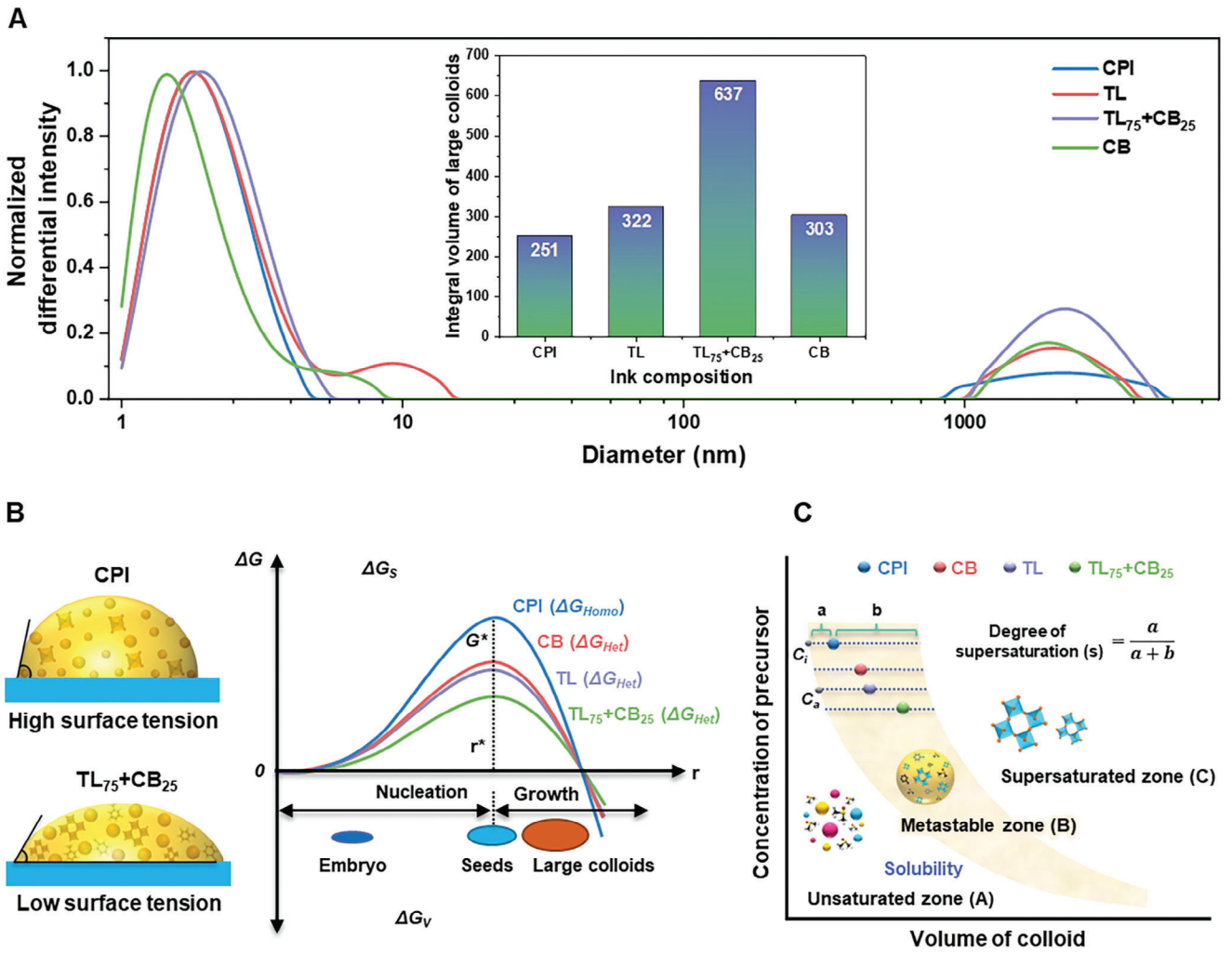

Figure 3. a) Colloidal size distribution of CPI and perovskite inks containing TL, TL_{75}+CB_{25}, and CB. b) Schematic illustration of the change in Gibbs free energy (ΔG) as a function of particle radius (r) during nucleation according to classical nucleation theory, where the volume term (G_V) and surface term (G_S) for ΔG, respectively. c) Phase diagram of the physical state of the CPI, CB, TL, and TL_{75}+CB_{25}-based colloidal ink.

an inhomogeneous morphology including pinholes, while the colloidal ink containing 12.5 vol% of TL_{75}+CB_{25} co-antisolvent allowed for a dense and uniform perovskite film with an appropriate thickness of ≈640 nm (Figure S14, Supporting Information). As a result, it can be concluded that the lower σ and η of the colloidal ink result in better wettability, forming a thicker and more uniform wet film, and eventually a high-quality perovskite film with proper thickness and no pinholes (Figure S15, Supporting Information). However, in the case of a too low σ and η, a dense and uniform thin film is formed with improved wettability (Figure S16, Supporting Information), but cracks occur in the process of forming a too-thick film (seen in Figure S7, Supporting Information), so it is necessary to formulate a colloidal ink containing an optimal antisolvent with an appropriate σ and η.

2.3. Crystallization Process of Colloidal Inks

The improved perovskite film in colloidal inks can be attributed to the addition of antisolvents with low surface tension and viscosity, which improved the rheological properties and film wettability of the ink. Additionally, it was postulated that this enhancement was due to the formation of colloidal-based supersaturated perovskite inks with low σ and η by the antisolvents TL or CB, which modulated perovskite nucleation and growth to favor having a dense and uniform morphology. To prove our hypothesis, dynamic light scattering (DLS) measurements were performed on colloidal inks containing TL or CB. As shown in **Figure 3a**, colloids with small and large diameters were found to exist in CPI as well as in colloidal inks containing CB or TL. However, CPI showed a low integral volume of large colloids, while colloidal inks containing TL or CB had relatively increased integral volumes, with TL+CB showing the highest integral volume of 637 (inset image of Figure 3a). This means that perovskite inks containing TL or CB form larger colloids, and the formation of large colloids is more promoted in perovskite inks containing both TL and CB. On the other hand, in Figure S17 (Supporting Information), it can be seen that large colloids are generated with increasing volumes of TL+CB, and it can be inferred that an appropriate amount of large colloid formation, rather than too

much, is required to form high-quality perovskite films. These results are consistent with the good perovskite film morphology and high-efficiency properties in the optimized colloidal ink containing 12.5 vol% of antisolvent in the ratio TL_{75}+CB_{25}, suggesting that the size and content of the colloid can be controlled by adjusting the content and ratio of the antisolvent, and through this, the crystallization process that determines the quality of the perovskite film can be controlled.

XRD analysis was performed to determine the effect of antisolvent (TL and CB) and the resulting colloids on perovskite crystallization in wet films (Figure S18, Supporting Information). It was confirmed that δ hexagonal phase perovskite was formed in the CPI-based wet film deposited by SD process, which indicates that the colloids observed in DLS are δ hexagonal phase perovskite. In the colloidal ink including CB, the formation of a small amount of new transitional intermediate phase (⊗) was observed with more δ hexagonal phase perovskite. Further, interestingly, in the colloidal ink including TL, the δ hexagonal phase perovskite was reduced, and a large amount of α cubic phase perovskite was newly formed, with an increase in the transitional intermediate phase. Lastly, it was observed that in colloidal inks including both TL and CB, the δ hexagonal perovskites disappeared and only α cubic perovskites and transitional intermediate phase were present. As a result, it can be seen that the incorporation of either TL or CB leads to the formation of perovskite seeds, i.e., colloids in the form of δ hexagonal phase, α cubic phase, and transitional intermediate phases, and that the incorporation of both TL and CB leads to the formation of large amounts of α cubic phase perovskite and transitional intermediate phases simultaneously, which can promote crystallization. Specifically, considering that the crystallization energy to crystallize from solution to the α cubic phase perovskite is larger compared to the activation energy required for the phase transition from the δ hexagonal phase perovskite to the α cubic phase perovskite (≈0.6-0.7 eV per f.u.),[29] it can be inferred that the crystallization of colloidal inks that already possess α cubic phase perovskite seeds and a transitional intermediate phase is more favorable.

The in-situ optical microscopy videos (Videos S1–S4, Supporting Information) showed clear and comprehensible evidence of the crystallization kinetics and film formation process of the colloidal perovskite inks. Figure S19 (Supporting Information) shows the images captured for the corresponding video as a function of time to better compare the crystallization and film formation processes. In the case of CPI, multiple crystal domains (t_{n+1s}, number of crystal domains > 36) appeared within a second of the first crystal domain being observed through nucleation (t_n), and the subsequent growth of the crystal domains formed a very large number of grains. Whereas, for colloidal inks containing TL and CB, a relatively small number of crystal domains were observed in t_{n+1s}, especially the smallest number of crystal domains and the resulting small number of grains in TL_{75}+CB_{25}. This can be inferred to be due to the formation of uniform and thick wet film by low surface tension and viscosity in colloidal inks containing TL or CB, and at the same time, large colloids with relatively low nucleation energy dominantly formed crystal domains and grew.

This crystallization process of perovskites can be explained through classical nucleation and growth theory.[30] Nucleation and growth are the primary steps involved in the formation of perovskite thin films. Once the solution attains a critical concentration and becomes supersaturated, it initiates nucleation in the perovskite solution, and external thermal energy then helps to promote the growth of perovskite crystals.[31] As an example, incorporating an antisolvent into the perovskite solution can serve as a catalyst to reach supersaturation and initiate the nucleation process.[32] In this study, the antisolvents, especially TL_{75}+CB_{25}, can produce higher level of supersaturation, leading to the formation of perovskite colloids (seeds), which is favorable to perovskite crystallization. As described in the previous section "Perovskite films and rheological properties", CPI exhibited high σ and η (with high θ), but colloidal inks containing TL or CB exhibited relatively low σ and η (with low θ). Therefore, rather than a homogeneous nucleation and growth mechanism, the crystallization process of colloidal inks may follow a heterogeneous nucleation and growth mechanism, which is considered using the following equation:[30]

$$\Delta G_{Het} = \Delta G_{Hom} \times f(\theta) \tag{1}$$

with

$$f(\theta) = \frac{(2 + cos\theta)(1 - cos\theta)^2}{4} \tag{2}$$

where, ΔG_{Het} represents the free energy required for heterogeneous nucleation, ΔG_{Hom} represents the free energy required for homogeneous nucleation, and θ represents the contact angle of perovskite ink. When θ decreases within the range $0° < \theta < 180°$, the $f(\theta)$ is decrease within the range $0 < f(\theta) < 1$, and consequently the ΔG_{Het} has lower value than the ΔG_{Hom}. From this relationship, it can be seen that the heterogeneous nucleation occurs in colloidal inks containing TL or CB, and the activation energy (ΔG^*) required for heterogeneous nucleation can be the minimum in TL_{75}+CB_{25}. Further, considering that the ΔG_{Het} for the perovskite nucleation can be expressed as follows,

$$\Delta G_{Het} = \left\{ -\frac{4}{3}\pi r^3 \Delta g + 4\pi r^2 \gamma \right\} \times f(\theta), (f(\theta) < 1 \tag{3}$$

it can be seen that ΔG_{Het} can be the lowest for colloidal ink containing TL_{75}+CB_{25}, which contains a lot of large colloids compared to other inks. Where r denotes the radius of the nucleus or colloids, Δg denotes the specific Gibbs free energy for solidification (crystal-free energy), and γ denotes the surface energy; if r is larger than some r^*(critical radius), an increase in r leads to a decrease in ΔG_{Het}, resulting in crystal growth. Consequently, it can be deduced that the magnitude of the ΔG^* required for perovskite crystallization decreases according to the volume of large colloids, in the order CPI, CB, TL, and TL_{75}+CB_{25} (Figure 3b), and that TL+CB, which has the lowest ΔG^*, may be more favorable for the formation of high-quality perovskite films with large grains. Moreover, the nucleation rate in the context of colloid-based heterogeneous nucleation, $\frac{dN}{dt}$, can be described by a modified Arrhenius-type equation[30,31]:

$$\frac{dN}{dt} = A \exp\left(-\frac{\Delta G^* f(\theta)}{K_B T} \right) \tag{4}$$

where N is the number of nuclei, t is time, A is the pre-exponential factor, $f(\theta)$ is the contact angle function ($0 < f(\theta) \leq 1$)

representing the interaction between the colloidal substrate and the nucleating phase, K_B is the Boltzmann constant, and T is temperature. In colloidal ink systems, it has been observed that inks containing larger colloids effectively lower the $\Delta G^* f(\theta)$ term, indicating a faster nucleation rate. However, to understand the actual phenomenon, which contradicts the fast nucleation and resulting small grain formation predicted by the previous equation, we must consider the concepts of Ostwald ripening and critical radius to account for the complexity of nucleation and growth during actual crystallization and thin film formation. Colloids larger than the critical radius tend to grow, a process further promoted by Ostwald ripening. The rate of Ostwald ripening, according to LSW (Lifshitz-Slyozov-Wagner) theory,[33] is expressed as:

$$\frac{dr}{dt} = K\left(\frac{1}{r^*} - \frac{1}{r}\right) \tag{5}$$

where K is the mass transfer constant. The magnitude of $(1/r^* - 1/r)$ determines how quickly the nuclei, or colloids, grow or shrink. Nuclei, or colloids, are much smaller than r^* will shrink rapidly, while those much larger than r^* will grow slowly. Larger colloids ($r > r^*$) have a lower surface energy and are less soluble; they tend to grow by incorporating the dissolved material from the smaller colloids or nuclei. Considering these mechanisms, we can explain the phenomena observed in inks containing larger colloids (i.e., TL_{75}+CB_{25}). Initially, the nucleation rate may increase due to the lowered $\Delta G^* f(\theta)$, but most of the large colloids are likely to have already exceeded the critical radius. Thus, these colloids primarily serve as bases for crystal growth rather than new nuclei formation. Through the Ostwald ripening process, smaller nuclei dissolve, and larger colloids grow further, resulting in the formation of fewer but larger grains. In contrast, in CPI, where numerous crystal grains were observed, we can infer; the initial colloid size distribution likely contained many colloids below a critical size, which promoted nucleation, the nucleation rate (dN/dt) was high enough to produce many nuclei before significant Ostwald ripening occurred, and the growth rate of the existing colloids was not fast enough to deplete supersaturation and prevent new nucleation. Thus, the overall crystal formation process can be thought of as a competition between nucleation and growth, and in CPI, conditions favored nucleation, leading to numerous small grains. In conclusion, the colloid-based heterogeneous nucleation process involves complex phenomena that cannot be described by a simple nucleation rate equation alone, and these complex processes lead to the formation of fewer nuclei and growth into larger particles despite the lower $\Delta G^* f(\theta)$ of colloidal inks. This is consistent with optical in-situ observation results (Figure S19, Supporting Information).

Up to this point, the process of perovskite crystallization in colloidal inks has been discussed through nucleation and growth theory in terms of the phase transition from liquid to solid, but in order to better explain the formation of perovskite films, the correlation between the supersaturation conditions of the solute in solution and the change in Gibbs free energy should be discussed. When the degree of supersaturation is defined as $S = C/C_s$ (where C is the solute concentration, C_s is the solubility limit, and $C > C_s$), the crystal-free energy for crystallization, Δg is dependent upon the T, k_B, S, and its molar volume v, Δg is defined in Equation (6).

$$\Delta g = \frac{-k_B T \ln(S)}{v} \tag{6}$$

Further, the ΔG^* can be expressed as a function of γ, v, and S, resulting in the following equation.

$$\Delta G^* = \frac{4}{3}\pi\gamma\,(r^*)^2 = \frac{4}{3}\pi\gamma\left(\frac{-2\gamma}{\Delta g}\right)^2 = \frac{16\pi v^2\gamma^3}{3k_B^2T^2(\ln S)^2} \tag{7}$$

From Equation (7), it can be seen that S should be increased to promote nucleation and growth by lowering. ΔG^*, and it is advantageous to allow the perovskite ink to reach supersaturation quickly to form a dense and pinhole-free perovskite film. From this perspective, perovskite inks containing TL or CB can reach supersaturation more quickly, and the colloids formed by reaching supersaturation, i.e., perovskite seeds, can promote nucleation and growth. Importantly, TL_{75}+CB_{25} provides the opportunity for critical saturation points to be reached more easily, and this supersaturation reduces the free energy of crystallization by forming perovskite seeds above the critical size, i.e., r^*, which acts as a driving force for the formation of high-quality perovskite thin films.

As discussed above, the complexity of perovskite crystallization is attributed to several variables, including concentration, surface tension, additives, and colloid formation. The phase diagrams shown in Figure 3c are a visual representation of the physical state of perovskite inks under various conditions, which can provide important information about the stability regions of different phases and the transitions between them, helping to understand the crystallization process of complex systems. The perovskite ink can be segmented into three primary zones[34]: (A) unsaturation zone, (B) the metastable zone that includes both fully dissolved and supersaturated state, and (C) the supersaturation zone. The solubility curve divides the zone of complete dissolution, A, and the zone of incomplete dissolution, B and C. Each point on this curve corresponds to a concentration, at which the solution is in equilibrium with the antisolvents. The antisolvent acts to weaken the perovskite-DMSO intermediate phase and lower its solubility, thus aiding perovskite nucleation, i.e., colloid formation, and further, the degree of supersaturation can be described by the traditional lever rule. The initial CPI ink is in a metastable zone close to the solubility limit, where the solubility is C_i, and the amount of solutions in the supersaturated state in the metastable zone can be represented by the leverage rule as a/(a+b). Thus, it can be inferred that a small volume of CPI in a supersaturated state can result in tiny amounts of colloids, which is consistent with the previous DLS results. Meanwhile, colloidal inks containing TL or CB antisolvents exist in a metastable zone near supersaturation, where the solubility is located at C_a. Accordingly, when the degree of supersaturation is calculated by the leverage rule, it can be seen that more solution is supersaturated compared to CPI, resulting in more colloids as shown in the DLS results. As a consequence, it can be inferred that in colloidal inks containing a large volume of supersaturation, the ΔG^* may be low, as shown in Equation (7), and that colloids enlarged above a

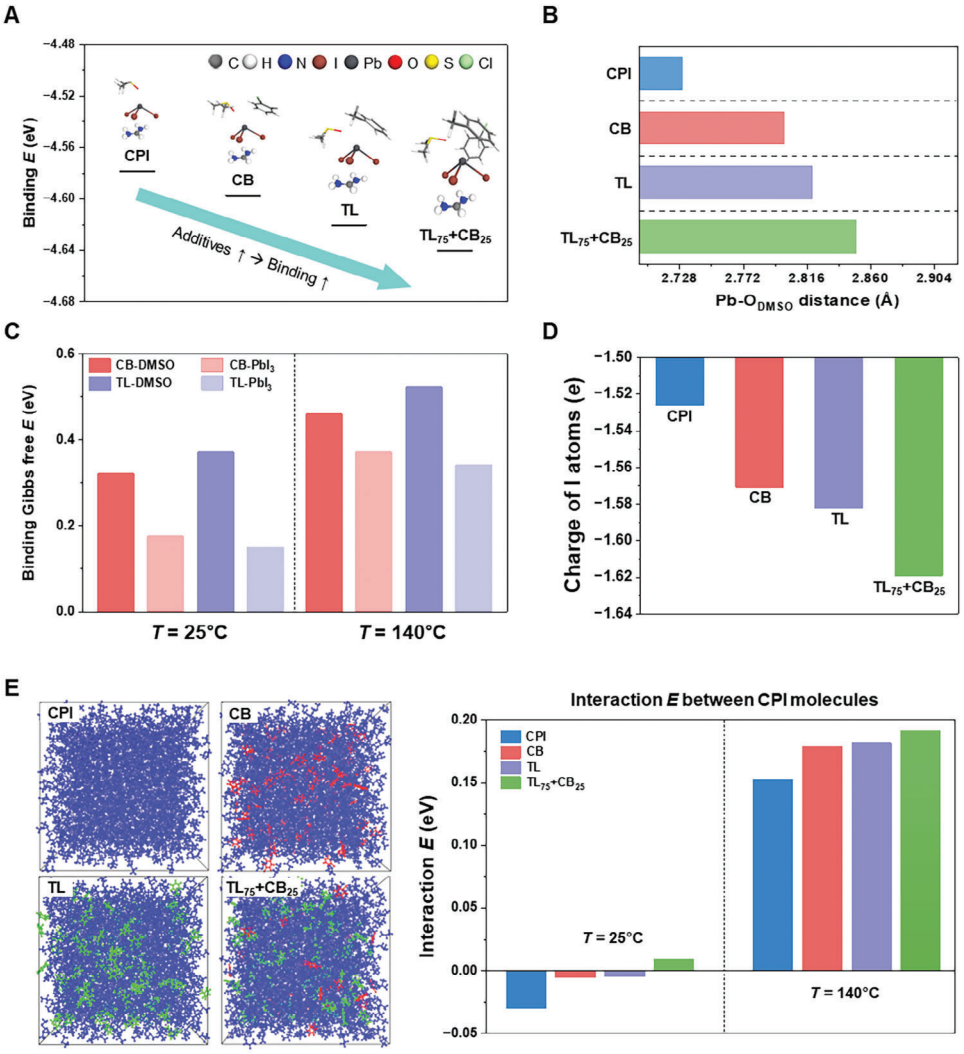

Figure 4. a) The binding energy of FA cation and PbI_3 anion in each condition. b) Distance between a lead atom of perovskite precursor and oxygen atom of CPI (DMSO). c) Binding Gibbs free energies of CB-DMSO, TL-DMSO, CB-PbI_3, and TL-PbI_3 in TL_{75}+CB_{25} system according to the temperature condition (i.e., 25 and 140 °C). d) Charge of I atoms in each condition. e) The interaction energy of CPI molecules in each condition at 25 °C/140 °C.

*r** grow more rapidly to crystals in the metastable state, forming large grains.[35]

Taken together, it can be concluded that for CPI with a low degree of supersaturation, some precursors form a small amount of colloids approaching the *r**, but as shown in Figure S20 (Supporting Information) (region I), perovskite crystallization requires overcoming *G** followed by nucleation and growth, resulting in the formation of small grains by multiple nucleation. Whereas, for colloidal inks containing TL and CB, where the colloid is larger than *r** (region II), crystallization proceeds immediately from the perovskite seeds (nucleation centers) as *G* is smaller than *G**, and crystal growth occurs spontaneously into large perovskite grains. Therefore, rheology and supersaturation control through the incorporation of antisolvents plays an important role in regulating the wettability and crystallization properties of colloidal inks, and control of colloid size and quantity is critical for the formation of high-quality perovskite films.

2.4. Computational Modeling and Interpretation

To understand the effects of CB and TL on the crystallization of perovskite structures, density functional theory (DFT) calculations were performed. We first investigated the binding energy between FA cation and PbI_3 anion in the CPI (DMSO), CB (DMSO+CB), TL (DMSO+TL), and TL_{75}+CB_{25} (DMSO+CB+TL) systems to understand the crystallization of the perovskite precursor induced by the CB and TL co-antisolvents as shown in **Figure** 4a. The binding energy was more thermodynamically favorable with the addition of antisolvent molecules (TL or CB), indicating the strong binding between the FA cation and PbI_3 anion. In particular, the combined with CB and TL additives showed the strongest binding energy, which was consistent with the increased distance between the lead atom of perovskite precursor and the oxygen atom of CPI (Figure 4b). These results suggest that additive molecules can strengthen the interaction

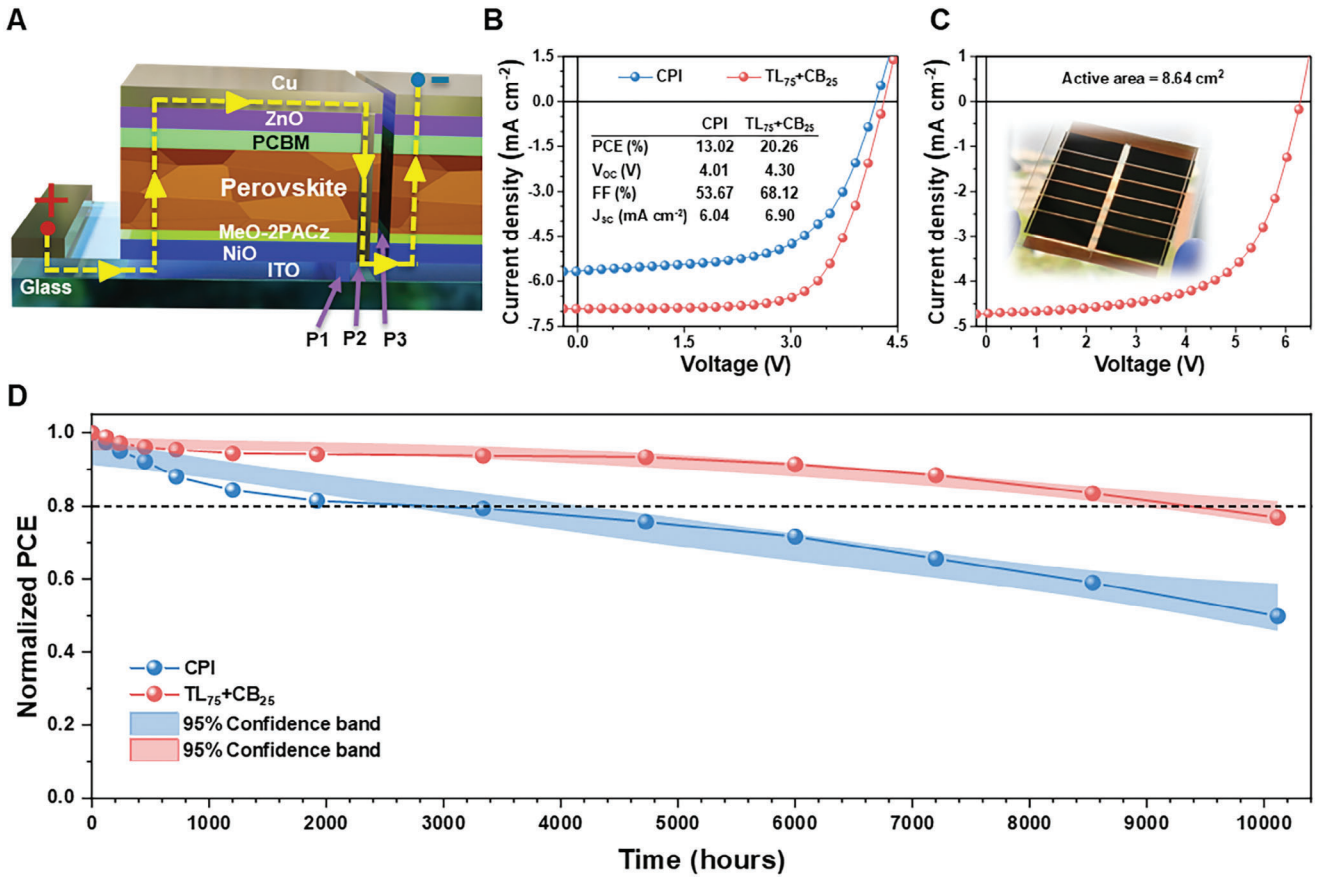

Figure 5. a) Schematic depicting the interconnection of a perovskite module fabricated through a typical scribing process. b) The *J–V* curve of the small-area minimodule measured under AM 1.5G illumination at 100 mW cm^{-2}. c) *J–V* curves of the convergence minimodule configured by connecting the upper and lower electrodes in parallel and the sub-cells in series. d) The long-term stability of unencapsulated unit cells based on CPI and TL_{75}+CB_{25} stored and measured for 10115 h in a nitrogen environment.

between perovskite precursors while simultaneously weakening the interaction of DMSO and PbI_2 in CPI inks. Furthermore, to explore the behavior at realistic coating temperatures, Gibbs free energy calculations were used to compare the interaction energies of CPI and inks incorporating CB or TL under experimental temperature conditions of 25 and 140 °C. The calculated binding Gibbs free energies for both CB and TL were positive, indicating repulsive interactions with the perovskite precursor, and their repulsive interactions were more enhanced as increasing the temperature (Figure 4c). This result substantiates the role of CB and TL as antisolvents. Furthermore, it can be inferred that the distance between the DMSO and Pb atoms can be increased. It could also weaken the coordination between DMSO and perovskite precursor and thereby strengthening the interaction between the components of perovskite precursor. Therefore, the co-antisolvents (i.e., CB and TL) can enhance repulsive interactions, which could further weaken the coordination bonding of DMSO to the perovskite precursor. Lastly, the charges of I atoms also showed more negative charges with introducing the co-antisolvents as shown in Figure 4d. Thus, we predicted that the co-antisolvents induced the electron accumulation of I atoms with the thermodynamically unstable of PbI_3 anion (Figure S21, Supporting Information), which strengthened the interaction with FA cation and improved the stability of the perovskite structure. Accordingly, the crystallization of the perovskite precursor can be favorable in the TL_{75}+CB_{25} system.

We next investigated the effects of CB and TL additives on the decrease of surface tension of CPI-based solutions by using the molecular dynamics (MD) simulations (Figure S22 and Table S8, Supporting Information). Figure 4e showed that the interaction between CPI molecules at 25 °C/140 °C became thermodynamically unfavorable with the introduction the antisolvent molecules. It indicates that the co-antisolvents can weaken the intermolecular interactions of CPI molecules, which results in decreasing the surface tension of perovskite solutions enabling the fabrication of uniform wet films. Overall, through the multiscale-based molecular simulations, we clarified the roles of CB and TL antisolvent molecules in the large formation of perovskite crystal structure (i.e., an increase of interaction of perovskite precursors and the decrease of surface tension of CPI solution).

2.5. Performance of Perovskite Solar Modules

As illustrated in **Figure** 5a, the minimodule was fabricated by series connection of 4 sub-cells with the same p-i-n

structure (ITO/NiO_x/MeO-2PACz/perovskite/$PC_{61}BM$/ZnO/Cu) as the unit cell. Figure S23 (Supporting Information) shows a lab-scale minimodule with an active area of 2.7 cm^2 fabricated by the SD process with TL_{75}+CB_{25} colloidal ink. The *J–V* curve for the lab-scale minimodule measured under AM 1.5G illumination at 100 mW cm^{-2} is presented in Figure 5b. The TL_{75}+CB_{25} colloidal ink-based lab-scale minimodule recorded a champion PCE of 20.26% under optimal conditions with a V_{OC} of 4.30 V, FF of 68.12, and J_{SC} of 6.90 mA cm^{-2}. The CPI-based minimodule, on the other hand, exhibited a lower PCE of 13.02% with a V_{OC} of 4.01 V, FF of 53.67, and J_{SC} of 6.04 mA cm^{-2}. This demonstrates that scaling from a single unit cell to a lab-scale minimodule is possible without performance degradation when using colloidal inks. Furthermore, as a step toward a commercial strategy, a convergence minimodule (5×5 cm^2) integrating serial and parallel interconnects was demonstrated, resulting in a champion PCE of up to 19.15% (V_{OC} of 6.34 V, FF of 63.48%, and J_{SC} of 4.65 mA cm^{-2}) on an active area of 8.64 cm^2 (Figure 5c). The results demonstrate that minimodules produced using colloidal ink (including TL and CB) and the SD process are competitive when compared to recent reports, as shown in Figure S24 (Supporting Information).[6,19–20,36] Additionally, we evaluated the uniformity and scalability of the perovskite film by applying our strategy to the fabrication of more substantial modules (Figure S25, Supporting Information). UV-vis spectral and PL mapping confirmed consistent light absorption and photoluminescence in random regions (A to C) of the large-area substrate (Figure S26, Supporting Information), and surface profile measurements confirmed uniform thickness (Table S9, Supporting Information), indicating that our approach could provide a promising pathway for the commercialization of perovskite solar cells.

Given that the stability of solar cells in real operating environments is one of the critical factors for commercialization, long-term stability, and light stability evaluations were performed on single-unit cells and minimodules. Figure 5d shows the long-term stability of representative unit cells produced with both CPI and colloidal ink including TL_{75}+CB_{25}, which were stored in a nitrogen environment for 10115 h without encapsulation (all *J–V* curves measured through the long-term stability evaluation can be found in Supporting Information; Figure S27, Supporting Information). At 10115 h, the colloidal ink (TL_{75}+CB_{25})–based unit cell retained 77% of its initial PCE, while the CPI-based unit cell retained only 50%. Even more surprisingly, for T_{80}, which refers to the time required to reach 80% efficiency from an initial efficiency value, the TL_{75}+CB_{25} showed excellent reliability with a long lifetime of ≈9400 h, a significant improvement over the CPI (T_{80} ≈ 2500 h). In addition, the colloidal ink (TL_{75}+CB_{25}) based lab-scale minimodule retained 86% of its initial PCE (T_{80} = 1200 h), demonstrating superior long-term stability compared to the CPI-based minimodule (43%, T_{80} = 480 h) (Figure S28, Supporting Information). Encouragingly, the unencapsulated CPI-based device retained only 47% (T_{80} = 120 h), while the colloidal ink (TL_{75}+CB_{25})-based device retained 73% (T_{80} = 500 h) of its PCE over 1000 h under 1 sun condition, demonstrating that colloidal ink-based devices may have better stability under real-world operating light (Figure S29, Supporting Information). Additionally, we conducted Maximum Power Point Tracking (MPPT) measurements under continuous 1 sun illumination at room temperature (Figure S30, Supporting Information). The TL_{75}+CB_{25}-based device maintained over 80% of its initial efficiency for more than 600 h under continuous operation. In contrast, the CPI-based device reached 27% of its initial efficiency before reaching 200 h. These findings demonstrate that TL_{75}+CB_{25}-based devices have better operational reliability. Long-term and operational stability were conducted according to the International Summit on Organic Photovoltaic Stability (ISOS) protocols, specifically ISOS-D-1I for dark aging, ISOS-L-1I for light stability, and ISOS-L-1 for MPPT stability.[37] These results emphasize that the devices fabricated via the colloidal ink developed through the incorporation of the antisolvents TL and CB and the SD process exhibit comparatively long-term operational stability.[20,38] This is attributed to the high-quality, pure-phase perovskite film with a dense, pinhole- and crack-free morphology originating from the colloidal ink is responsible for the excellent stability, as derived from the previous analysis.

3. Conclusion

In summary, this study demonstrated the high-efficiency, highly stable PSCs and minimodules using an SD process based on colloidal inks incorporating TL and CB as co-antisolvents. The colloidal ink including TL_{75}+CB_{25} exhibited superior rheological properties compared to CPI, with low surface tension (38.52 mN m^{-1}) and viscosity (26.93 cP), leading to improved wettability and the formation of a high-quality perovskite film. DLS measurements revealed the formation of large colloids in the colloidal ink, especially TL_{75}+CB_{25}, promoting heterogeneous nucleation and lowering the activation energy (ΔG^*) for crystallization. DFT calculations further demonstrated that the incorporation of TL_{75}+CB_{25} led to the strongest binding energy between the FA cation and PbI_3 anion, making the crystallization process more thermodynamically favorable and enhancing perovskite stability. This resulted in enhanced crystal growth and superior crystallinity, as confirmed by XRD analysis and microscopic observations. The optimized colloidal ink yielded devices with a maximum efficiency of 21.32% and remarkable long-term stability, retaining 77% of initial efficiency over 10115 h. It also demonstrated excellent scalability, achieving 20.26% efficiency for 2.7 cm^2 lab-scale minimodules and 19.15% for 8.64 cm^2 convergence minimodules. These results provide insight into the intricate relationship between ink composition, rheological properties, film quality, crystallization kinetics, and device performance, demonstrating that colloidal ink-based SD process is a promising approach for the commercialization of high-efficiency, highly stable perovskite solar cells and modules.

Supporting Information

Supporting Information is available from the Wiley Online Library or from the author.

Acknowledgements

This work was supported by the National Research Foundation of Korea (NRF) grant funded by the Korean government (MSIT) (NRF-2021R1A2C2010353, RS-2023-00207836, and RS-2023-00246239) and the Korea Electric Power Corporation (CX72220014). This work was also supported by the Glocal University 30 Project Fund of Gyeongsang National University in 2024.

Conflict of Interest

The authors declare no conflict of interest.

Data Availability Statement

The data that support the findings of this study are available from the corresponding author upon reasonable request.

Keywords

antisolvent, colloidal ink, crystallization kinetics, modules, perovskite solar cells, slot-die process

Received: December 20, 2024
Revised: January 21, 2025
Published online:

[1] a) M. Grätzel, *Nat. Mater.* **2014**, *13*, 838; b) N.-G. Park, M. Grätzel, T. Miyasaka, K. Zhu, K. Emery, *Nat. Energy* **2016**, *1*, 16152; c) J. J. Yoo, G. Seo, M. R. Chua, T. G. Park, Y. Lu, F. Rotermund, Y.-K. Kim, C. S. Moon, N. J. Jeon, J.-P. Correa-Baena, *Nature* **2021**, *590*, 587; d) S. De Wolf, J. Holovsky, S.-J. Moon, P. Loper, B. Niesen, M. Ledinsky, F.-J. Haug, J.-H. Yum, C. Ballif, *J. Phys. Chem. Lett.* **2014**, *5*, 1035.

[2] T. Bu, L. K. Ono, J. Li, J. Su, G. Tong, W. Zhang, Y. Liu, J. Zhang, J. Chang, S. Kazaoui, *Nat. Energy* **2022**, *7*, 528.

[3] S. Y. Abate, Y. Qi, Q. Zhang, S. Jha, H. Zhang, G. Ma, X. Gu, K. Wang, D. Patton, Q. Dai, *Adv. Mater.* **2024**, *36*, 2310279.

[4] P. Shi, Y. Ding, B. Ding, Q. Xing, T. Kodalle, C. M. Sutter-Fella, I. Yavuz, C. Yao, W. Fan, J. Xu, *Nature* **2023**, *620*, 323.

[5] a) M. Du, S. Zhao, L. Duan, Y. Cao, H. Wang, Y. Sun, L. Wang, X. Zhu, J. Feng, L. Liu, *Joule* **2022**, *6*, 1931. b) M. Kim, J. Jeong, H. Lu, T. K. Lee, F. T. Eickemeyer, Y. Liu, I. W. Choi, S. J. Choi, Y. Jo, H.-B. Kim, *Science* **2022**, *375*, 302.

[6] Z. Yang, W. Zhang, S. Wu, H. Zhu, Z. Liu, Z. Liu, Z. Jiang, R. Chen, J. Zhou, Q. Lu, *Sci. Adv.* **2021**, *7*, eabg3749.

[7] Y. Zang, Y. Tu, C. Jiao, W. Li, P. Zhou, J. Cheng, G. Yang, T. Shao, J. Ye, G. Li, *Chem. Eng. J.* **2024**, *480*, 148133.

[8] a) Z. Xing, X. Meng, D. Li, T. Hu, X. Hu, Y. Chen, *Sci. Bull.* **2022**, *67*, 561; b) K. Yan, M. Long, T. Zhang, Z. Wei, H. Chen, S. Yang, J. Xu, *J. Am. Chem. Soc.* **2015**, *137*, 4460; c) H. Zhao, X. Liu, J. Xu, Z. Li, Y. Fu, H. Zhu, L. Yan, Z. Liu, S. F. Liu, J. Yao, *ACS Appl. Mater. Interfaces* **2020**, *12*, 48756.

[9] J. Li, J. Dagar, O. Shargaieva, M. A. Flatken, H. Köbler, M. Fenske, C. Schultz, B. Stegemann, J. Just, D. M. Többens, *Adv. Energy Mater.* **2021**, *11*, 2003460.

[10] a) X. Zhang, D. Han, X. Chen, Y. Chen, S. Chang, H. Zhong, *Acta Phys. Chim. Sin* **2021**, *37*, 2008055; b) S. Rahimnejad, A. Kovalenko, S. M. Forés, C. Aranda, A. Guerrero, *ChemPhysChem* **2016**, *17*, 2795.

[11] Y. Zhang, Y. Wang, X. Yang, L. Zhao, R. Su, J. Wu, D. Luo, S. Li, P. Chen, M. Yu, *Adv. Mater.* **2022**, *34*, 2107420.

[12] N. Sun, S. Fu, Y. Li, L. Chen, J. Chung, M. M. Saeed, K. Dolia, A. Rahimi, C. Li, Z. Song, Y. Yan, *Adv. Funct. Mater.* **2023**, *34*, 2309894.

[13] H. Zhang, K. Darabi, N. Y. Nia, A. Krishna, P. Ahlawat, B. Guo, M. H. S. Almalki, T.-S. Su, D. Ren, V. Bolnykh, *Nat. Commun.* **2022**, *13*, 89.

[14] Y. Deng, C. H. Van Brackle, X. Dai, J. Zhao, B. Chen, J. Huang, *Sci. Adv.* **2019**, *5*, aax7537.

[15] C. Chen, J. Chen, H. Han, L. Chao, J. Hu, T. Niu, H. Dong, S. Yang, Y. Xia, Y. Chen, *Nature* **2022**, *612*, 266.

[16] H. Li, C. Zuo, D. Angmo, H. Weerasinghe, M. Gao, J. Yang, *Nano-Micro Lett.* **2022**, *14*, 79.

[17] a) Z. Li, T. R. Klein, D. H. Kim, M. Yang, J. J. Berry, M. F. Van Hest, K. Zhu, *Nat. Rev. Mater.* **2018**, *3*, 18017; b) Y. Galagan, F. Di Giacomo, H. Gorter, G. Kirchner, I. de Vries, R. Andriessen, P. Groen, *Adv. Energy Mater.* **2018**, *8*, 1801935.

[18] F. Bisconti, A. Giuri, G. Marra, A. Savoini, P. Fumo, R. Marrazzo, S. Zanardi, G. Corso, R. Po, P. Biagini, *ChemPlusChem* **2021**, *86*, 1442.

[19] J. Li, J. Dagar, O. Shargaieva, O. Maus, M. Remec, Q. Emery, M. Khenkin, C. Ulbrich, F. Akhundova, J. A. Márquez, *Adv. Energy Mater.* **2023**, 2203898.

[20] S. S. Sangale, S. N. Kwon, P. Patil, H. J. Lee, S. I. Na, *Adv. Energy Mater.* **2023**, *13*, 2300537.

[21] a) X. Huang, G. Deng, S. Zhan, F. Cao, F. Cheng, J. Yin, J. Li, B. Wu, N. Zheng, *ACS Cent. Sci.* **2022**, *8*, 1008; b) P. Nath, A. Ray, *Nano Express* **2024**, 5.

[22] M.-J. Choi, Y.-S. Lee, I. H. Cho, S. S. Kim, D.-H. Kim, S.-N. Kwon, S.-I. Na, *Nano Energy* **2020**, *71*, 104639.

[23] Y.-J. Kang, S.-I. Na, *Nano Energy* **2022**, *97*, 107193.

[24] a) J. Cao, X. Jing, J. Yan, C. Hu, R. Chen, J. Yin, J. Li, N. Zheng, *J. Am. Chem. Soc.* **2016**, *138*, 9919; b) D. R. Wargulski, K. Xu, H. Hempel, M. A. Flatken, S. Albrecht, D. Abou-Ras, *ACS Appl. Mater. Interfaces* **2023**, *15*, 41516.

[25] P. Patil, S.-N. Kwon, S. S. Sangale, D. S. Mann, S.-I. Na, *J. Mater. Chem. A* **2023**, *11*, 26636.

[26] M. E. Schrader, *Langmuir* **1995**, *11*, 3585.

[27] C. Caddeo, D. Marongiu, S. Meloni, A. Filippetti, F. Quochi, M. Saba, A. Mattoni, *Adv. Mater. Interfaces* **2019**, *6*, 1801173.

[28] a) A. Ali, M. J. Cha, J. H. Kang, Y. J. Park, J. H. Seo, B. Walker, *Adv. Eng. Mater.* **2020**, *22*, 2000185; b) E. C. S. Mahen, F. A. Permatasari, O. Floweri, B. W. Nuryadin, M. A. Irham, S. Z. Bisri, A. H. Aimon, F. Iskandar, *J. Lumin.* **2022**, *248*, 118954.

[29] a) M. Li, R. Sun, J. Chang, J. Dong, Q. Tian, H. Wang, Z. Li, P. Yang, H. Shi, C. Yang, Z. Wu, R. Li, Y. Yang, A. Wang, S. Zhang, F. Wang, W. Huang, T. Qin, *Nat. Commun.* **2023**, *14*, 573; b) Y. Liang, F. Li, X. Cui, T. Lv, C. Stampfl, S. P. Ringer, X. Yang, J. Huang, R. Zheng, *Nat. Commun.* **2024**, *15*, 1707.

[30] N. T. Thanh, N. Maclean, S. Mahiddine, *Chem. Rev.* **2014**, *114*, 7610.

[31] S. Karthika, T. Radhakrishnan, P. Kalaichelvi, *Cryst. Growth Des.* **2016**, *16*, 6663.

[32] S. Ghosh, S. Mishra, T. Singh, *Adv. Mater. Interfaces* **2020**, *7*, 2000950.

[33] a) Z. Wu, S. Sang, J. Zheng, Q. Gao, B. Huang, F. Li, K. Sun, S. Chen, *Angew. Chem., Int. Ed.* **2024**, *63*, 202319170; b) B. Zhou, P. Zhao, J. Guo, Y. Qiao, S. Hu, X. Guo, J. Liu, C. Li, *Nano Energy* **2024**, *124*, 109487.

[34] a) K.-M. Lee, C.-J. Lin, B.-Y. Liou, S.-M. Yu, C.-C. Hsu, V. Suryanarayanan, M.-C. Wu, *Sol. Energy Mater. Sol. Cells* **2017**, *172*, 368; b) A. Bijelic, A. Rompel, *ChemTexts* **2018**, *4*, 10.

[35] a) A. C. Dumetz, A. M. Chockla, E. W. Kaler, A. M. Lenhoff, *Biophys. J.* **2008**, *94*, 570; b) G. E. Dale, C. Oefner, A. D'Arcy, *J. Struct. Biol.* **2003**, *142*, 88.

[36] a) S. H. Huang, C. K. Guan, P. H. Lee, H. C. Huang, C. F. Li, Y. C. Huang, W. F. Su, *Adv. Energy Mater.* **2020**, *10*, 2001567; b) M. Du, X. Zhu, L. Wang, H. Wang, J. Feng, X. Jiang, Y. Cao, Y. Sun, L. Duan, Y. Jiao, *Adv. Mater.* **2020**, *32*, 2004979; c) D. Lee, Y.-S. Jung, Y.-J. Heo, S. Lee, K. Hwang, Y.-J. Jeon, J.-E. Kim, J. Park, G. Y. Jung, D.-Y. Kim, *ACS Appl. Mater. Interfaces* **2018**, *10*, 16133; d) Y. Lv, K. Wang, A. Lan, L. Chao, C. Chen, J. Wang, Q. Yao, J. Chen, T. Pan, Y. Li, H. Zhang, Y. Xia, Y. Chen, *Chem. Eng. J.* **2023**, *469*, 143909; e) Y. F. Shen, H. Zhang, J. Zhang, C. Tian, Y. Shi, D. Qiu, Z. Zhang, K. Lu, Z. Wei, *Adv. Mater.* **2023**, *35*, 2209030; f) E. Bi, W. Tang, H. Chen, Y. Wang, J. Barbaud, T. Wu, W. Kong, P. Tu, H. Zhu, X. Zeng, *Joule* **2019**, *3*, 2748; g) C. Huang, C.-K. Guan, B.-Q. Lin, S.-H. Huang, B.-J. Huang, W.-F. Su, L. Xu, *Sol. RRL* **2023**, *7*, 2200945; h) D. Yang, M. Ma, Y. Li, G. Xie, Y. Ma, S. Wu, C. Liu, *Chem. Commun.* **2023**, *59*, 1521.

[37] B. Li, K. I. Jayawardena, J. Zhang, R. M. I. Bandara, X. Liu, J. Bi, S. M. Silva, D. Liu, C. C. Underwood, Y. Xiang, *Renewable Sustainable Energy Rev.* **2024**, *189*, 114002.

[38] a) S. S. Sangale, D. S. Mann, H.-J. Lee, S.-N. Kwon, S.-I. Na, *Commun. Mater.* **2024**, *5*, 201; b) X. Jiang, C. Li, X. Wang, C. Peng, H. Jiang, H. Bu, M. Zhu, H. Yin, B. He, H. Li, *ACS Energy Lett.* **2023**, *8*, 1068.